Macromolecules
ARTICLE

Macromolecules **2010**, *43*, 3359–3364 **3359**
DOI: 10.1021/ma902780p

Crystallization Kinetics of Poly(ethylene oxide) in Confined Nanolayers

Haopeng Wang, Jong K. Keum, Anne Hiltner,* and Eric Baer

Department of Macromolecular Science and Engineering, Case Western Reserve University,
Cleveland, Ohio 44106-7202

Received December 19, 2009; Revised Manuscript Received February 24, 2010

ABSTRACT: A new approach for imposing long-range, defect-free confinement was used to study the crystallization kinetics of ultrathin polymer layers. Layer multiplying coextrusion was utilized to create films in which hundreds or thousands of continuous microlayers or nanolayers of a crystallizable polymer were separated by layers of a rigid confining polymer. Even in confined layers as thin as a single lamella, isothermal crystallization of poly(ethylene oxide) followed the conventional habit whereby chains folded back and forth in the crystal with a common fold surface free energy and fold length. However, the crystallization rate was substantially suppressed even when the layer thickness was tens of micrometers, a thickness scale where the well-known substrate effect must have been negligible. The crystallization kinetics was modeled by considering the effect of truncation when the growing spherulite encountered the interface. Although crystallization was dramatically retarded as the layers became thinner, the Avrami equation, expressed for heterogeneously nucleated bulk crystallization of polymers, was valid for thin and ultrathin confined films.

Introduction

Long-chain molecules can crystallize, and they do so for the same energetic reasons as low-molecular-weight materials. The main characteristic of crystalline polymers that distinguishes them from most other crystalline solids is that they are normally only semicrystalline. Single crystals grown from solution are usually in the form of isolated lamellae or platelets having thickness on the order of 10−20 nm and lateral dimensions on the order of micrometers. The chains fold back and forth in a more-or-less orderly way. The folds regions give rise to a noncrystalline component. When crystallized from the quiescent melt, the lamellae arrange themselves in 3 dimensions along the radial directions from a central nucleus. The interlamellar regions of the spherulite are composed of amorphous or noncrystallizable fractions of the polymer. The crystallization of polymers is of enormous technological importance. Most thermoplastic polymers are processed from the melt and crystallize to some extent when the molten polymer is cooled below the melting point. There are many factors that can affect the rate and extent to which crystallization occurs for a particular polymer. They can be processing variables such as the cooling rate, the presence of orientation in the melt, and the melt temperature.

The requirements of nanoscience and nanotechnology for the fabrication of ultrathin polymer layers pose special challenges for polymer crystallization. The thickness of ultrathin polymer layers, usually a few tens of nanometers, is comparable to or smaller than the lamellar crystal thickness or the radius of gyration R_g. Because the conventional 3-dimensional crystal growth is frustrated, crystallization in such confinement can produce unique crystal orientations.[1−10] In contrast to bulk crystallization from the melt, which usually initiates at heterogeneous nuclei such as catalyst residues, high molecular weight gel particles, or dust particles, crystallization in ultrathin layers or films usually initiates by homogeneous nucleation.

Measurements are typically performed on a coated substrate with a free surface where it is reported that the growth rate decreases, often by multiple orders of magnitude.[2,11,12] However, film thickness is not the only factor affecting the rate and extent of crystallization in thin films. Because the glass transition temperature (T_g) and the molecular mobility can be greatly altered due to the interaction at the interface between substrate and polymer, transport of polymer chain segments to the crystal growth front is affected. In block copolymers, a reduction in the effective diffusion coefficient affects the crystallization rate of PEO blocks confined by covalent links to glassy PS blocks.[13] Only a small amount of material is obtained with most of the methods used to fabricate ultrathin films. This usually limits the measurements to either nucleation rate or growth rate, and the overall crystallization rate cannot be readily assessed in a single experiment.

We recently innovated a process for obtaining ultrathin polymer layers with true 1-dimensional confinement.[14] The exceptional flexibility and control of the crystallization conditions allows access to the temperature domain that encompasses the transition from homogeneous nucleation to heterogeneous nucleation even in layers as thin as 25 nm.[15] Despite the nanoscale confinement, crystallization follows the conventional process whereby polymer chains fold back and forth into stems and form crystalline lamellae even when the layer thickness is comparable to R_g.[16] Here we probe the regime of heterogeneous nucleation by studying the isothermal crystallization kinetics of poly(ethylene oxide) (PEO) layers. The confining polymer is (PS), which provides a noninteracting interface from which the PEO dewets.[17] Layer multiplying coextrusion is used to create films in which hundreds or thousands of continuous microlayers or nanolayers of a crystallizable polymer are subjected to long-range, almost defect-free confinement.[18,19] Although the amount of material in a single layer is very small, the properties of the confined layer are multiplied manyfold by the number of identical layers in the film. This enables us to probe the kinetics of confined crystallization using conventional thermal analysis methods.

Experimental Section

Materials. Poly(ethylene oxide) (PEO) with a molecular weight of 200 kg/mol (PolyOx WSR N-80) and polystyrene

*Corresponding author. E-mail: ahiltner@case.edu.

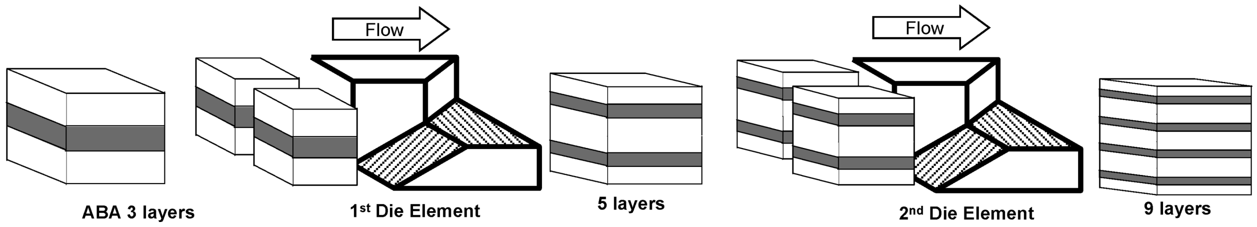

Figure 1. Layer-multiplying coextrusion for forced-assembly of polymer nanolayers. After the polymer melts are combined in the ABA feedblock, the melt stream flows through a series of layer-multiplying die elements; each element splits the melt vertically, spreads it horizontally, and finally recombines it with twice the number of layers. The figure illustrates how two elements multiply the number of layers from 3 to 9. An assembly of n die elements produces $2^{(n+1)} + 1$ layers with outer layers of polymer A. Finally, the melt is spread in a film die to further reduce the layer thickness.

Table 1. Characteristics of Extruded PS/PEO Films

	PS/PEO composition			nominal layer thickness (nm)					
number of layers	(vol %/vol %)	(wt %/wt %)	film thickness (μm)	PS	PEO	$T_{\mathrm{m,PEO}}$ (°C)	$\Delta H_{\mathrm{m,PEO}}$ (J/g)	$X_{\mathrm{c,PEO}}$ (wt %)	$T_{\mathrm{c,PEO}}$ (°C)
PS	100/0	100/0	127						
PEO	0/100	0/100	127			65	150	76	45
9	70/30	72/28	284	50000	21000	66	147	75	44
256	50/50	49/51	254	1000	1000	65	142	72	44
256	70/30	72/28	127	700	300	64	140	71	42
1025	70/30	72/28	128	175	75	64	148	75	40
1025	90/10	91.4/8.6	117	214	25	64	133	68	40

(PS) (STYRON 666D, MFI = 8.0, 200 °C/5.0 kg, ASTM D1238) were obtained from The Dow Chemical Company. Both PS and PEO were dried under vacuum before processing. Films with alternating PS and PEO layers were fabricated using the layer multiplication process, as shown in Figure 1.[20,21] The extruder, multiplier elements, and die temperatures were set to 200 °C to ensure matching viscosities of the two polymer melts. Films with 9, 257, and 1025 alternating PS and PEO layers with PS outer layers were coextruded. In order to obtain the target PEO layer thicknesses, the relative thicknesses of the PS and PEO layers were also varied by adjusting the feed ratio to the extruders as (PS/PEO) (v/v) 50/50, 70/30, and 90/10 for two film thicknesses of about 250 and 125 μm. The nominal layer thickness was calculated from the number of layers, the composition ratio, and the film thickness (Table 1). Nonlayered PS and PEO control films were also extruded. The films were stored at ambient temperature in desiccators to prevent moisture absorption.

Differential Scanning Calorimetry. Thermograms were obtained on a Perkin-Elmer (Boston, MA) Series 7 differential scanning calorimeter (DSC) at a heating/cooling rate 10 °C min^{-1}. For isothermal crystallization, specimens were melted at 90 °C. At this temperature, the PEO was melted, but the PS remained in the rigid glassy state and maintained the layer integrity. The specimen was held at 90 °C for 5 min and rapidly cooled at 100 °C min^{-1} to the crystallization temperature (T_x). A new specimen was used for each isothermal test. The number of lids in the reference pan was adjusted to minimize the time required to achieve a stable instrumental baseline.[22]

Atomic Force Microscopy. The isothermally crystallized films were embedded in epoxy and cured at room temperature. Cross sections were microtomed at −80 °C perpendicular to the extrusion direction with a cryo-ultramicrotome (MT6000-XL from RMC, Tucson, AZ). The cross sections were examined with an atomic force microscope (AFM) in order to visualize the layers and the layer morphology. Phase and height images of the cross sections were recorded simultaneously at ambient temperature in air using the tapping mode of the Nanoscope IIIa MultiMode scanning probe (Digital Instruments, Santa Barbara, CA). In all cases, the AFM images revealed the layers to be continuous. There was some variation in the layer thickness; however, the average layer thickness corresponded closely to the nominal layer thickness calculated from the number of layers, the film thickness, and the composition ratio.

X-ray Scattering. The small-angle X-ray scattering (SAXS) measurements were carried out using a rotating anode X-ray generator (RU 300, 12 kW, Rigaku, Woodlands, TX) equipped with two laterally graded multilayer optics in a side-by-side arrangement, giving a highly focused parallel beam of monochromatic Cu Kα radiation ($\lambda = 0.154$ nm). The monochromatic X-ray beam operated at 40 kV and 80 mA was collimated using three pinholes; the diameter of the X-ray beam at the sample position was ~700 μm. SAXS patterns were obtained by aligning the incident X-ray beam along the direction of film plane (PD) and the normal direction (ND) of the film. For the collection PD SAXS patterns, since the thickness of the films (50−250 μm) was smaller than the collimated X-ray beam, the X-ray beam was aligned at an angle of ~3° relative to PD to avoid total reflection. The critical angle for the total reflection was usually on the order of a few tenths of a degree. On the other hand, in order to collect ND SAXS patterns, the X-ray beam was aligned parallel to the ND. Two-dimensional (2D) SAXS patterns were collected by using a 2D gas filled multiwire detector (Rigaku) with a spatial resolution of 1024 × 1024 pixels. The X-ray exposure time for PD and ND SAXS patterns was 9 h. The sample-to-detector distance was 1.5 m, and the scattering vector s was calibrated using a silver behenate (AgBe) standard, which had (001) peak position at $s = 0.171$ nm^{-1}. Here, the scattering vector s is defined as $s = |\vec{s}| = 2\lambda^{-1}\sin\theta$, where λ is the wavelength of the X-ray beam and θ is half of the scattering angle. A photodiode beam stop placed in front of the area detector allowed monitoring of the intensity of the direct beam. Based on the intensity of the direct beam, all SAXS images were corrected for background scattering and sample absorption. The WAXD measurements were performed using the same rotating anode X-ray generator. The PD and ND WAXD patterns were collected with the monochromatic X-ray beam parallel to PD and ND. The collimated beam size was ~0.5 mm. The 2D wide-angle X-ray diffraction (WAXD) patterns were collected with a Bruker AXS (Madison, WI) HI-STAR area detector. The sample-to-detector distance was 74 mm, and the diffraction angle was calibrated using a CaF_2 standard.

Results and Discussion

Structure of Isothermally Crystallized PEO Layers. The heating thermogram of a film with 25 nm PEO layers showed

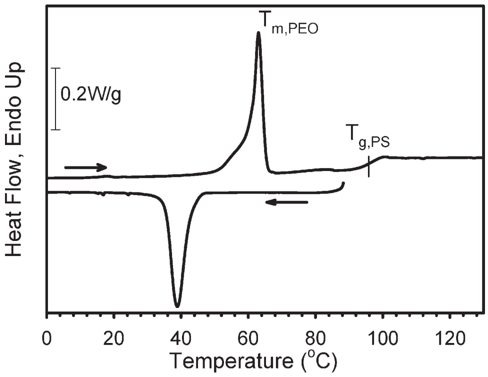

Figure 2. DSC thermogram of the PS/PEO 90/10 film with 1025 alternating layers and nominal PEO layer thickness of 25 nm. The heating curve was collected by heating a specimen from −10 to 150 °C. The cooling curve was collected by cooling another specimen after it was heated only to 90 °C and held at 90 °C for 5 min. The heating/cooling rate was 10 °C/min.

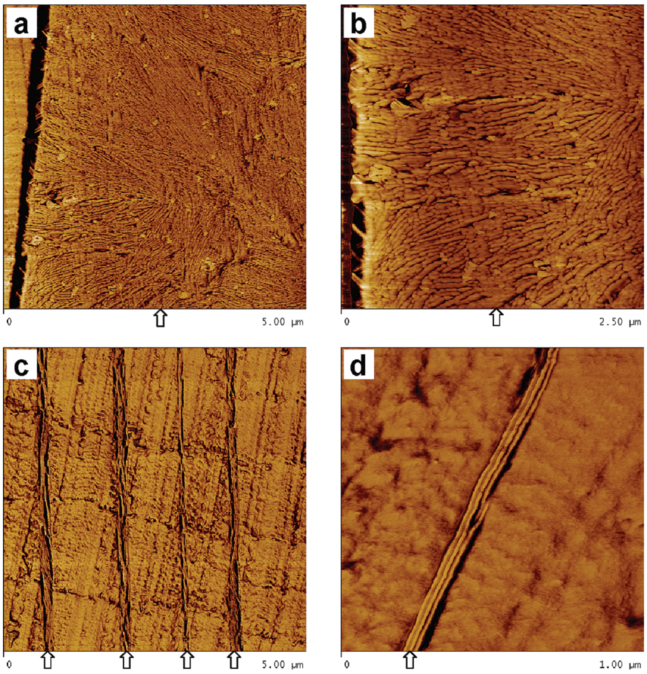

Figure 3. AFM phase images of partial cross sections of PS/PEO layered films: (a, b) A film with nine alternating layers and nominal PEO layer thickness of 21 µm and (c, d) 1025 alternating layers and nominal PEO layer thickness of 75 nm. The scale bars are as indicated and the arrows indicate the PEO layers. The films were crystallized isothermally at T_x = 53 °C.

a PEO melting endotherm at 65 °C ($T_{m,PEO}$) and a baseline inflection for the PS glass transition at 98 °C ($T_{g,PS}$) (Figure 2). The PEO melting temperature and the PEO crystallinity ($X_{c,PEO}$) of about 75% did not vary much with layer thickness (Table 1). There was a temperature window between $T_{m,PEO}$ and $T_{g,PS}$ where the PEO layers melted within the confinement of rigid glassy PS layers. A film with 25 nm PEO layers was taken to 90 °C to melt the PEO layers and subsequently cooled at 10 °C/min. The recrystallization exotherm appeared at 40 °C ($T_{c,PEO}$), only 5 °C lower than a PEO control (Figure 2). A crystallization temperature of the nanolayers close to that of the bulk and much higher than that of homogeneous nucleation, reportedly between −10 and 0 °C,[17] indicated that crystallization of the PEO layers nucleated on heterogeneous nuclei even when the layer was only 25 nm thick.

The confined PEO layers were melted at 90 °C and isothermally crystallized at T_x in the temperature range of 49 °C ≤ T_x ≤ 55 °C. At T_x = 53 °C, the crystallization habit of 21 µm PEO layers closely resembled that of PEO in the bulk with radial growth of 25 nm thick lamellar stacks (Figure 3a,b). The lateral dimension of the spherulite-like structures was about 160 µm, which was considerably larger than the layer thickness. These truncated structures were better described as discoids. In contrast, the continuous 75 nm thick PEO layers consisted of stacks of three to five lamellae whose length exceeded the 1 µm scale of the image (Figure 3c,d). The crystallization habit systematically changed from truncated lamellar spherulites in micrometer-thick layers to single lamellae that resembled large single crystals with a very high degree in-plane orientation in 25 nm nanolayers.[14]

The WAXD pattern with the beam parallel to the plane of the film (PD) revealed the (120) reflections at the equator and the (032) reflections at azimuthal ϕ = 67°, 113°, 237°, and 293° (Figure 4a), indicating that the *c*-axis was predominantly vertical to the layer plane. Crystallization of 25 nm layers as in-plane lamellae was due to the narrow confinement in the PS layer interstices and was facilitated by the correspondence between the layer thickness and the lamellar thickness of PEO. As the confinement was relaxed by increasing the PEO layer thickness, the spots broadened into arcs. In the ND WAXD patterns, isotropic rings indicated that the lamellae were randomly oriented in the plane of the layer (not shown).

The PD SAXS patterns showed meridional scattering maxima indicating that the main scattering vector of the in-plane lamellae was normal to the layer (Figure 4b). The peak positions remained nearly the same regardless of the layer thickness (Figure 4c). The long period, L_p, obtained from the first-order meridional scattering maxima (s_{max}), $L_p = 1/s_{max}$, was 26.3 ± 0.4 nm. In 25 nm layers with thickness comparable to L_p, the first-order peak maximum in the SAXS pattern was much weaker than that from thicker layers. If the lamellae were uncorrelated within the PEO layers, they should not have shown a first-order peak maximum in the SAXS pattern but an asymptotic decay. It was thought that the observed weak lamellar correlation peak from 25 nm PEO layers was associated with the thickness distribution of the layers which occasionally enabled formation of two lamellae in a single PEO layer. Although similar to the crystalline morphologies observed in as-extruded films,[16] the isothermally crystallized PEO layers were more highly ordered with larger spherulitic entities in the thick layers and longer lamellae with improved in-plane orientation in the thin layers.

Isothermal Crystallization Kinetics. The question arose whether or not crystallization of the single lamellae in nanolayers followed the conventional kinetics habit. The isothermal DSC curves for all the layered films showed a single peak as is typical for isothermal polymer crystallization. The relative crystallinity X_t, defined as the ratio of crystallinity at time *t* to the crystallinity when time approaches infinity, is given as

$$X_t = \Delta H_t/\Delta H_\infty = \int_0^t (\mathrm{d}H\ \mathrm{d}t)\ \mathrm{d}t \Big/ \int_0^\infty (\mathrm{d}H/\mathrm{d}t)\ \mathrm{d}t \qquad (1)$$

where $\mathrm{d}H/\mathrm{d}t$ is the rate of heat evolution, ΔH_t is the total heat evolved at time *t*, and ΔH_∞ (Table 2) is the total heat evolved as time approaches infinity. Plots of the relative crystallinity as a function of time showed the sigmoidal shape, as is typical of isothermal polymer crystallization. Representative plots

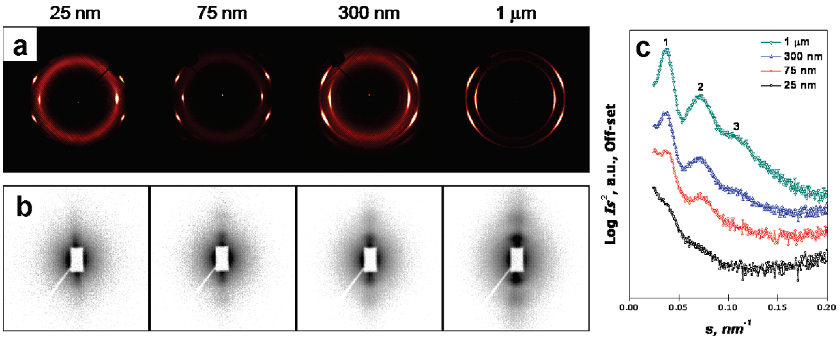

Figure 4. (a) WAXD patterns, (b) SAXS patterns, and (c) SAXS meridional scans of PS/PEO films with 25 nm, 75 nm, 300 nm, and 1 μm PEO layer thicknesses isothermally crystallized at $T_x = 50$ °C.

Table 2. Results of Isothermal Crystallization and Avrami Analysis

PEO layer thickness (μm)	T_x (°C)	$t_{1/2}$ (min)	ΔH_∞ (J/g)	n	K (min^{-n})
PEO 127 (control film)	53	1.90	140	2.4	0.17
	54	3.21	144	2.4	0.059
	55	6.46	144	2.4	0.0088
21	51	1.28	35	2.0	0.36
	52	2.31	37	2.0	0.14
	53	3.76	36	1.9	0.060
	54	7.46	37	1.8	0.020
1.0	50	2.02	67	2.0	0.18
	51	3.25	67	1.9	0.077
	52	4.74	68	1.9	0.036
	53	8.25	72	1.9	0.014
	54	14.81	66	1.9	0.0041
0.30	49	1.72	35	2.0	0.24
	50	2.62	36	1.8	0.12
	51	4.30	36	1.8	0.052
	52	6.75	37	1.9	0.019
	53	12.41	37	1.8	0.0073
0.075	49	2.18	36	1.9	0.19
	50	3.52	37	1.9	0.074
	51	5.88	40	1.7	0.030
	52	8.47	40	1.8	0.012
	53	16.17	40	1.8	0.0050
0.025	49	3.28	12	1.8	0.083
	50	4.61	13	1.8	0.043
	51	8.04	12	1.9	0.015
	52	13.02	13	1.8	0.0076
	53	20.20	12	1.8	0.0025

at $T_x = 53$ °C showed that the overall crystallization rate was retarded as the layer thickness decreased (Figure 5a).

Polymer crystallization by heterogeneous nucleation typically follows a temperature dependence described by[23]

$$\ln t_{1/2} = \frac{4\sigma\sigma_e b_0 T_m^\circ}{\Delta H^\circ \rho_c \kappa_B} \frac{1}{T_x \Delta T} + \text{const} \qquad (2)$$

where σ and σ_e, the specific side and fold surface free energies, measure of work required to create a new surface; ΔH° (206 J/g) and T_m° (69 °C), ρ_c (1.33 g/cm^3), b_0 (4.65×10^{-10} m), and $\Delta T = T_m^\circ - T_x$ are the heat of melting of PEO crystals, the equilibrium melting temperature, the density of the PEO crystal, the diameter of the polymer chain in the crystal, and the thermal driving force for crystallization, respectively.[24] The common temperature dependence of $t_{1/2}$, as indicated by the parallel linear plots in Figure 5b, signified that the geometric constraint did not alter the crystallization mechanism. Rather, lamellar crystallization in nanolayers followed the conventional crystallization habit, responding to the same kinetic factors as spherulitic crystallization of the PEO control. Regardless of PEO layer thickness, a common value of the product $\sigma\sigma_e = 3.1 \times 10^{-4}$ J^2/m^4

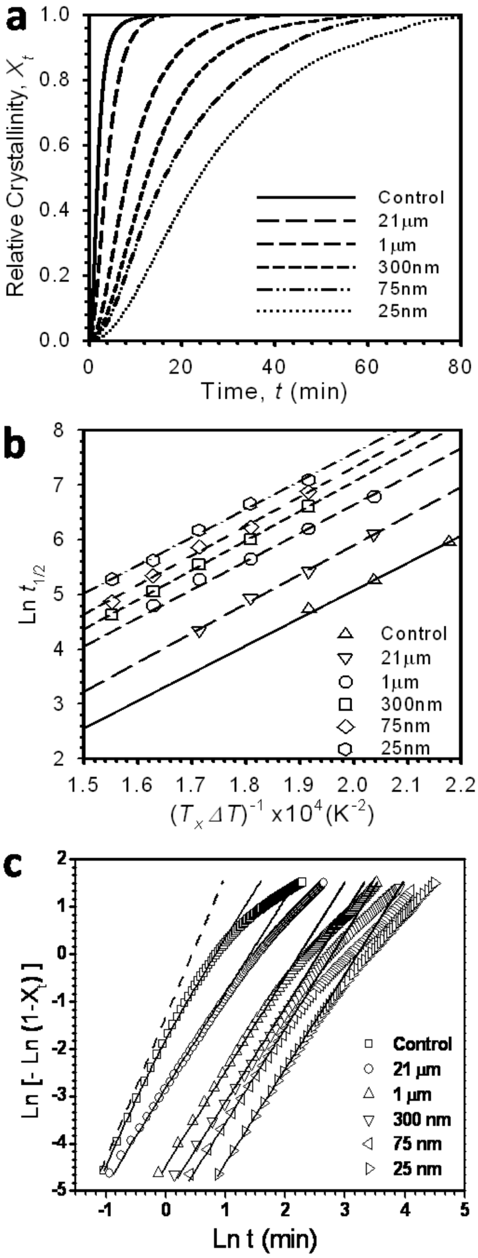

Figure 5. (a) Relative crystallinity of PEO layers (X_t) versus time (t) for isothermal crystallization at 53 °C. (b) Crystallization half-time ($\ln t_{1/2}$) versus the thermal driving force ($1/T_x\Delta T$) for isothermal crystallization at 53 °C. (c) Avrami plots for isothermal crystallization at 53 °C. The solid lines are the fits from eqs 3 and 4. The dashed line represents the calculated three-dimensional growth of PEO with $d \rightarrow \infty$ using eq 3.

was extracted from the slope value of $(5.2 \pm 0.15) \times 10^4$. This was in good agreement with literature values of $(2.7-7.2) \times 10^{-4}$ J^2/m^4.[23,24] A typical value for σ of 1.0×10^{-2} J/m^2[25] resulted in $\sigma_e = 3.1 \times 10^{-2}$ J/m^2.[26] The work of chain folding, q, was then estimated as $q = 2\sigma_e b_0$. A value of $q \sim 1.9$ (kcal/mol folds) was similar to that in the literature.[26] A common value of q meant that chain folding proceeded irrespective of layer confinement. With identical melting temperature regardless of PEO layer thickness (Table 1), the common q also implied that the critical nucleus size, calculated from $l^* = 2\sigma_e T_m^\circ/(\Delta H_\infty \rho_c \Delta T)$ as ~5 nm at $T_x = 53$ °C, was identical for all layer thicknesses.

The crystallization kinetics at $T_x = 53$ °C is plotted in Figure 3c according to the classic Avrami equation,[27] $\ln[-\ln(1 - X_t)] = n \ln t + \ln k$, where k is the crystallization rate constant and n is the Avrami exponent describing the crystal growth geometry and nucleation mechanism. The early stage of crystallization was linear in the Avrami plot, but a gradual deviation from linearity was observed at higher X_t. For consistency, the slope n and the intercept $\ln k$ were taken from the linear portion between $X_t = 0.05$ and $X_t = 0.5$. Confining PEO in 25 nm layers decreased the crystallization rate constant k by almost 2 orders of magnitude (Table 3). It was noteworthy that n took on an integer value in the confined layers of 2.0 indicative of 2-dimensional growth.

The crystallization rate was substantially suppressed even when the layer thickness was in micrometers, a thickness scale where the substrate effect must have been negligible. Some other explanation for the reduction in crystallization rate was sought. Models that describe the effect of confinement on spherulitic crystallization kinetics predict substantial reductions in both the crystallization rate and the Avrami exponent when the film thickness is less than the average size of the spherulite. The PEO nanolayers provided an opportunity to test the models, which, to our knowledge, had not been done previously. Haudin and co-workers modeled the crystallization kinetics of thin polymer films (thickness in micrometers) by considering the truncation when the growing spherulite encounters the interface.[28] Schultz developed a comparable model by expunging the effects of spherulites that would have existed beyond the surfaces of the film.[29] The detailed derivation is reported in the literature,[28] and only a brief description is given here. For a thin confined layer with thickness d, the relative crystallinity X_t for instantaneous heterogeneous nucleation can be calculated from the radial growth rate of the spherulite G_0 and the initial number of potential nuclei per unit volume N_v as follows:

when $t \leq d/G_0$:

$$X_t = 1 - \exp\left[-\frac{4}{3}\pi N_v {G_0}^3 t^3 \left(1 - \frac{3G_0}{8\,d}t\right)\right] \tag{3}$$

when $t \geq d/G_0$:

$$X_t = 1 - \exp\left[-\pi N_v d\left({G_0}^2 t^2 - \frac{d^2}{6}\right)\right] \tag{4}$$

with three parameters G_0, N_v, and d. It should be noted that the model can give noninteger values of the Avrami exponent n. The model was fit to the crystallization kinetics in Figure 5a, and the resulting Avrami plots are compared in Figure 5c.

Table 3. Nucleation Density and Growth Rate from Isothermal Crystallization at 53 °C

PEO layer thickness, d (μm)	nucleation density[a] $N_v \times 10^8$ (μm^{-3})	area nucleation density[b] $N_A \times 10^8$ (μm^{-2})	growth rate[c] G_0 (μm s^{-1})	n
110 (control)	5.9	649	1.7	2.4
21	6.2	130	2.0	2.0
1	35	35	4.2	2.0
0.3	55	17	5.4	2.0
0.075	145	11	8.6	2.0
0.025	200	5	10.0	2.0

[a] $G_0 = 1.7$ μm s^{-1}. [b] $N_A = N_v d$. [c] $N_v = 5.9 \times 10^{-8}$ μm^{-3}.

Data for the PEO control film were fit first. A value of 5.9×10^{-8} μm^{-3} for N_v gave a final average spherulite radius close to the observed size of about 160 μm. For the control, d and G_0 were adjusted to obtain the best fit of the experimental data for X_t less than 0.5. The fit gave $d = 110$ μm, which was close to the thickness of the PEO film that was used as the control. The fit gave the radial growth rate as 1.7 μm s^{-1}, in good agreement with the reported value for PEO at this temperature,[30] and an Avrami exponent of 2.4. This nonintegral exponent less than 3 seemed incompatible with the 3D growth of spherulites under athermal nucleation and suggested that spherulite growth was truncated to some extent even in the control. Indeed, the average spherulite radius (160 μm) in the control film crystallized at 53 °C exceeded the film thickness (110 μm). The Avrami plot for the unconfined, 3D crystallization of PEO was constructed using N_v and G_0 from the control film. The result is included as the dashed line in Figure 5c. The rate constant k was 0.27 min^{-n}, compared to 0.17 min^{-n} in the control film, with an exponent n of 3.

For the layered films, d was taken as the nominal thickness of the PEO layers. Using the value of G_0 obtained from the control as constant, N_v was adjusted to give the best fit to the data for the 21 μm layers. The resulting N_v was essentially the same as the control value (Table 3), and the Avrami exponent was 2. Thus, the slower crystallization rate of the 21 μm thick PEO layers compared to the PEO control and the reduction in the Avrami exponent were fully accounted for by the layer thickness d, without adjusting the other parameters. Note that the layer thickness was well below the spherulite radius of ~160 μm calculated from N_v and observed experimentally.

When the layer thickness was reduced to 1 μm or less, the model parameters obtained from the PEO control predicted a crystallization rate that was considerably slower than the observed rate. The magnitude of the deviation was systematic and logarithmic with the layer thickness. It was possible to obtain a satisfactory fit by increasing N_v and/or G_0. Diffusion of additional heterogeneous nuclei from the thick confining PS layer could have increased N_v. Energetic advantages favored concentration of impurities at the layer interfaces. Indeed, it was noted that except in very thick layers, crystallization tended to nucleate at the interface.[16] Concentration of additional heterogeneous nuclei at the interface would have become more important as the PEO layers were made thinner and the melt contact time increased. Assuming that G_0 remained constant and equal to G_0 of the control, only N_v was adjusted to obtain the results in Figure 5c. Good fits with the experimental data for $X_t \leq 0.5$ were obtained giving the Avrami exponent as 2 for all the layered films regardless of the layer thickness. The area density of nuclei in the PEO layer defined as $N_A = N_v d$ is included with N_v in Table 3. Even if N_v increased substantially as the layers become thinner, N_A decreased by 2 orders of magnitude.

The low N_A facilitated formation of the very large lamellae observed in the thin and ultrathin layers.

Although it was unlikely that G_0 increased as the layers became thinner,[2,11,12] the possibility was considered. A recent study showed that cylindrical confinement with radius thinner than R_g can reduce the intermolecular entanglement density due to the decreased pervaded volume of the chains and thereby enhance chain mobility.[31] Because of the decreased intermolecular entanglement, a single chain or a few-chain compact globule can crystallize faster than the bulk.[32] The root-mean-square radius of gyration can be estimated as[33]

$$\langle R_g{}^2\rangle^{1/2} = C(n_w{}^{1/2}) \tag{5}$$

with C being the characteristic ratio of 0.272 nm based on small-angle neutron scattering for the PEO melt and n_w is the weight-averaged number of monomer units per molecule. The estimated $\langle R_g{}^2\rangle^{1/2}$ was about 18 nm for PEO chains with $M_w = 200$ kg/mol, or comparable to d of the thinnest PEO layers. Assuming that N_v remained constant and equal to N_v of the control, adjusting only G_0 in the fitting process also gave good fits. An increase in G_0 by a factor of about 6 compared to the control was required to fit the experimental data for the thinnest PEO layers (Table 3).

Conclusions

The effect of confinement on the crystallization habit of polymers impacts a variety of technologies that require the use of crystalline polymers as ultrathin films and layers. Layer-multiplying coextrusion, which operates with readily available crystallizable polymers, offers a powerful new approach to studying confined crystallization. Here, we present one of the first studies of heterogeneously nucleated crystallization in confined nanolayers. By systematically decreasing the layer thickness from the microscale to the nanoscale, we provide a new and straightforward explanation for the decrease in crystallization rate that is based on nucleation density and qualitatively described by the Haudin model.

Acknowledgment. This research was supported by the NSF Center for Layered Polymeric Systems (Grant DMR-0423914).

References and Notes

(1) Douzinas, K. C.; Cohen, R. E. *Macromolecules* **1992**, *25*, 5030.
(2) Bartczak, Z.; Argon, A. S.; Cohen, R. E.; Kowalewski, T. *Polymer* **1999**, *40*, 2367.
(3) Zhang, Y.; Mukoyama, S.; Hu, Y.; Yan, C.; Ozaki, Y.; Takahashi, I. *Macromolecules* **2007**, *40*, 4009.
(4) Schönherr, H.; Frank, C. W. *Macromolecules* **2003**, *36*, 1188.
(5) Sutton, S. J.; Izumi, K.; Miyaji, H.; Miyamoto, Y.; Miyashita, S. *J. Mater. Sci.* **1997**, *32*, 5621.
(6) Bu, Z.; Welch, M. B.; Ho, R.-M.; Zhou, W.; Jangchud, I.; Eby, R. K.; Cheng, S. Z. D.; Hsieh, E. T.; Johnson, T. W.; Geerts, R. G. *Macromolecules* **1996**, *29*, 6575.
(7) Abe, H.; Kikkawa, Y.; Iwata, T.; Aoki, H.; Akehata, T.; Doi, Y. *Polymer* **1999**, *41*, 867.
(8) Mareau, V. H.; Prud'homme, R. E. *Macromolecules* **2005**, *38*, 398.
(9) Sun, Y. S.; Chung, T. M.; Li, Y. J.; Ho, R. M.; Ko, B. T.; Jeng, U. S.; Lotz, B. *Macromolecules* **2006**, *39*, 5782.
(10) Ho, R. M.; Lin, F. H.; Tsai, C. C.; Lin, C. C.; Ko, B. T.; Hsiao, B. S.; Sics, I. *Macromolecules* **2004**, *37*, 5985.
(11) Massa, M. V.; Dalnoki-Veress, K.; Forrest, J. A. *Eur. Phys. J. E* **2003**, *11*, 191.
(12) Schönherr, H.; Frank, C. W. *Macromolecules* **2003**, *36*, 1199.
(13) Zhu, L.; Cheng, S. Z. D.; Calhoun, B. H.; Ge, Q.; Quirk, R. P.; Thomas, E. L.; Hsiao, B. S.; Yeh, F. J.; Lotz, B. *J. Am. Chem. Soc.* **2000**, *122*, 5957.
(14) Wang, H. P.; Keum, J. K.; Hiltner, A.; Baer, E.; Freeman, B.; Rozanski, A.; Galeski, A. *Science* **2009**, *323*, 757.
(15) Wang, H.; Keum, J. K.; Hiltner, A.; Baer, E. *Macromol. Rapid Commun.* **2010**, *31*, 356.
(16) Wang, H.; Keum, J. K.; Hiltner, A.; Baer, E. *Macromolecules* **2009**, *42*, 7055.
(17) Massa, M. V.; Dalnoki-Veress, K. *Phys. Rev. Lett.* **2004**, *92*, 255509/1.
(18) Liu, R. Y. F.; Jin, Y.; Hiltner, A.; Baer, E. *Macromol. Rapid Commun.* **2003**, *24*, 943.
(19) Liu, R. Y. F.; Bernal-Lara, T. E.; Hiltner, A.; Baer, E. *Macromolecules* **2004**, *37*, 6972.
(20) Mueller, C. D.; Nazarenko, S.; Ebeling, T.; Schuman, T. L.; Hiltner, A.; Baer, E. *Polym. Eng. Sci.* **1997**, *37*, 355.
(21) Bernal-Lara, T. E.; Ranade, A.; Hiltner, A.; Baer, E. Nano- and Microlayered Polymers: Structure and Properties. In *Mechanical Properties of Polymers Based on Nanostructure*, 1st ed.; Micheler, G. H., Balta-Callaja, F., Eds.; CRC Press: Boca Raton, FL, 2005; p 629.
(22) Hu, Y. S.; Rogunova, M.; Schiraldi, D. A.; Hiltner, A.; Baer, E. *J. Appl. Polym. Sci.* **2002**, *86*, 98–115.
(23) Wunderlich, B. *Macromolecular Physics*; Academic Press: New York, 1976; Vol. *2*.
(24) Vyazovkin, S.; Stone, J.; Sbirrazzuoli, N. *J. Therm. Anal. Calorim.* **2005**, *80*, 177.
(25) Alfonso, G. C.; Russell, T. P. *Macromolecules* **1986**, *19*, 1143.
(26) Wu, L.; Lisowski, M.; Talibuddin, S.; Runt, J. *Macromolecules* **1999**, *32*, 1576.
(27) Avrami, M. *J. Chem. Phys.* **1939**, *7*, 1103.
(28) Escleine, J. M.; Monasse, B.; Wey, E.; Haudin, J. M.; et al. *Colloid Polym. Sci.* **1984**, *262*, 366.
(29) Schultz, J. M. *Macromolecules* **1996**, *29*, 3022.
(30) Cheng, S. Z. D.; Wunderlich, B. *J. Polym. Sci., Part B: Polym. Phys.* **1986**, *24*, 595.
(31) Shin, K.; Obukhov, S.; Chen, J.-T.; Huh, J.; Hwang, Y.; Mok, S.; Dobriyal, P.; Thiyagarajan, P.; Russell, T. P. *Nat. Mater.* **2007**, *6*, 961.
(32) Gu, F.; Bu, H. *Macromol. Rapid Commun.* **1999**, *20*, 595.
(33) Kugler, J.; Fischer, E. W. *Makromol. Chem.* **1983**, *184*, 2325–2334.